Imaging mRNA and protein interactions within neurons

Carolina Eliscovich[a], Shailesh M. Shenoy[a,b], and Robert H. Singer[a,b,c,1]

[a]Department of Anatomy and Structural Biology, Albert Einstein College of Medicine, Bronx, NY 10461; [b]Gruss Lipper Biophotonics Center, Albert Einstein College of Medicine, Bronx, NY 10461; and [c]Howard Hughes Medical Institute, Janelia Research Campus, Ashburn, VA 20147

Contributed by Robert H. Singer, January 3, 2017 (sent for review December 9, 2016; reviewed by Arjun Raj, John W. Sedat, and Xiaowei Zhuang)

RNA–protein interactions are essential for proper gene expression regulation, particularly in neurons with unique spatial constraints. Currently, these interactions are defined biochemically, but a method is needed to evaluate them quantitatively within morphological context. Colocalization of two-color labels using wide-field microscopy is a method to infer these interactions. However, because of chromatic aberrations in the objective lens, this approach lacks the resolution to determine whether two molecules are physically in contact or simply nearby by chance. Here, we developed a robust super registration methodology that corrected the chromatic aberration across the entire image field to within 10 nm, which is capable of determining whether two molecules are physically interacting or simply in proximity by random chance. We applied this approach to image single-molecule FISH in combination with immunofluorescence (smFISH-IF) and determined whether the association between an mRNA and binding protein(s) within a neuron was significant or accidental. We evaluated several mRNA-binding proteins identified from RNA pulldown assays to determine which of these exhibit bona fide interactions. Surprisingly, many known mRNA-binding proteins did not bind the mRNA in situ, indicating that adventitious interactions are significant using existing technology. This method provides an ability to evaluate two-color registration compatible with the scale of molecular interactions.

super registration | chromatic aberration correction | smFISH-IF

RNA-binding proteins (RBPs) specifically recognize and bind with RNA, regulating its lifecycle (1, 2). Dysfunctional RNA–protein interaction represents one of the causes of genetic disorders that vary from neurodevelopmental and neurodegenerative diseases to cancer (3–9). Traditionally, RNA–protein interactions have been investigated by ensemble biochemistry approaches, including affinity purification and cross-linking and immunoprecipitation-based techniques (reviewed in refs. 10 and 11). However, these methods may report adventitious RNA–protein associations that would occur after lysis of cells (12, 13), or functionally important complexes may not survive the procedure. Importantly, ensemble biochemistry studies lack morphological information, particularly essential for neurons.

Currently, there is no method to verify whether these biochemical techniques determine real interactions that take place in the cell. Standard wide-field microscopy has been used to reveal interactions by "colocalizing" two fluorescent tags. Technically, "colocalization" refers to two or more fluorescent molecules emitting different wavelengths of light that superimpose within an indeterminate microscopic resolution. Biologically, colocalization implies the association between these molecules. However, their physical association occurs at a dimension not usually achievable by light microscopy because it occurs below the diffraction limit (~250 nm). Thus, as currently practiced, colocalization is a suggestion of spatial correlation but does not rule out random association. Here, we derive a method to define colocalization precisely as a nonrandom physical association of two labels at a resolution consistent with their molecular dimensions. We used fluorescent beads with sizes below the diffraction limit of light to determine the characteristics of the objective and derived a correction algorithm to coregister their centers of each point spread function (PSF) at different wavelengths across the field of view (FOV) with nanometer precision, a process that we refer to as "super registration."

We tested the method using proteins known to bind mRNA in hippocampal neurons. Specifically, we used β-actin and spinophilin mRNAs and two proteins that have been previously shown to bind to them: an endogenous protein [zipcode binding protein 1 (ZBP1)] (14–17) and an engineered protein that binds the MS2 binding sites (MBSs) inserted into the 3′-UTR of β-actin mRNA [MS2 Capsid Protein (MCP)] (18, 19). As a negative control, we used an mRNA that binds neither of these two proteins. We used these controls to develop a method to assess the significance of binding. We then tested whether RBPs isolated biochemically with a standard RNA pulldown met the binding test developed using this quantitative microscopic approach. The results show that, by using standard light microscopy, we can identify with high probability whether these putative binding proteins actually interact with the mRNA and how much. The approach is applicable to any two-labeled molecular species. Significantly, any standard fluorescence microscope can achieve this super registration methodology by simple calibration of the objective lens coupled with subsequent image analysis. This approach provides the quality control for the information obtained from biochemistry techniques.

Results

Super Registration. We developed a dual-color methodology that reduced systematic errors limiting previous colocalization measurements by rigorously characterizing the microscope optics (*Materials and Methods* and *SI Results*). We first imaged subdiffraction-limited fluorescent beads with a broad emission spectrum in *z* stacks and detected sequentially in Cy5 and Cy3 channels (Fig. 1*A*). The centroids of these beads were determined with subpixel precision (20). We calculated the displacement vectors

Significance

Gene expression is regulated by interactions between mRNAs and RNA-binding proteins. This functionality depends on their ability to specifically recognize and bind RNAs within the cell. Thus, elucidation of RNA–protein interactions is an area of active research. Technological developments allowed the study of these associations in living cells by ensemble biochemistry approaches. However, these traditional methods to investigate RNA–protein association may report adventitious associations and importantly, lack information about cellular spatial information. In this work, we provide an approach that can integrate information from biochemical interactions with visualization of these physical contacts within neurons.

Author contributions: C.E. and R.H.S. designed research; C.E. performed research; C.E. and S.M.S. contributed new reagents/analytic tools; C.E. and S.M.S. analyzed data; and C.E. and R.H.S. wrote the paper.

Reviewers: A.R., University of Pennsylvania; J.W.S., University of California, San Francisco School of Medicine; and X.Z., Harvard University/Howard Hughes Medical Institute.

Conflict of interest statement: The material in this manuscript is the subject of a provisional application to the US Patent and Trademark Office. It has not been licensed to any corporation, and the authors are the sole inventors.

Freely available online through the PNAS open access option.

[1]To whom correspondence should be addressed. Email: robert.singer@einstein.yu.edu.

This article contains supporting information online at www.pnas.org/lookup/suppl/doi:10.1073/pnas.1621440114/-/DCSupplemental.

between the centroid positions of each bead in the two channels as a function of its position in the field (Fig. 1 *B* and *C*). This process revealed that the chromatic aberration varied substantially from the center of the field to the edge (by as much as 120 nm) (Fig. 1 *C* and *D*) because of the inability of the planapochromatic objective lens to correct across the entire field. To compensate for this aberration, we developed a transform that reduced the error to less than 10 nm across the entire FOV (Fig. 1*E*, *SI Results*, and Fig. S1).

Imaging Physical Contact Between MBS-Containing β-Actin mRNA and MCP. To provide a standard model system for calibration of protein binding, we used mRNA tagged with MBS (19) to visualize single mRNA molecules and their associated RBPs within fixed cells. Neurons derived from a mouse in which 24 MBSs were integrated into the 3′-UTR of the β-actin gene were cultured in vitro for 14–21 d (18). The fluorescent capsid protein MCP-GFP was introduced by lentivirus infection and specifically binds to MBS

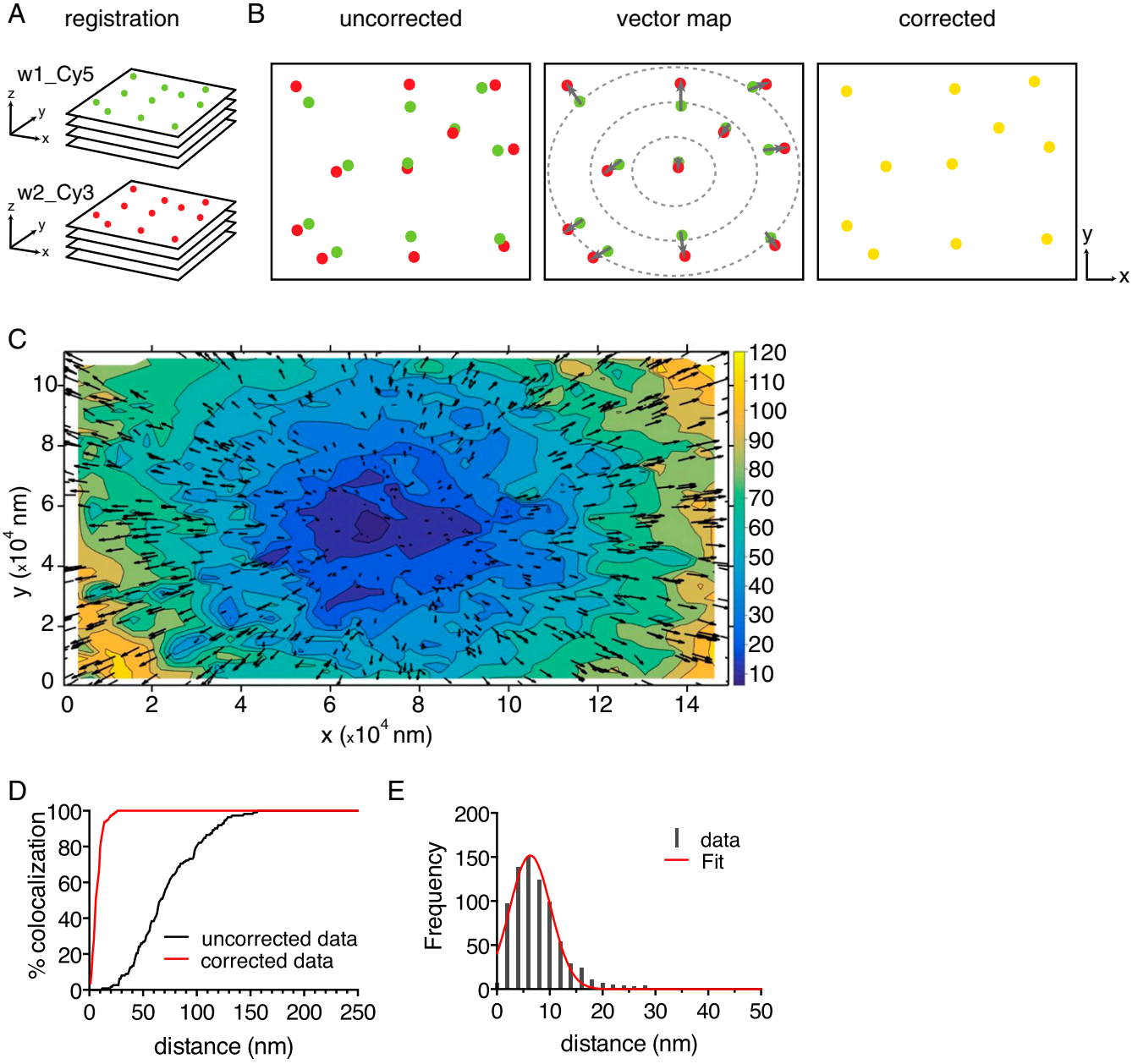

Fig. 1. Super registration procedure for dual-color localization microscopy. (*A*) Registration. A poly–L-lysine–coated surface was sparsely loaded with 100-nm-diameter fluorescent beads, and *z* stacks were acquired in Cy5 (green) and Cy3 (red) channels with a wide-field microscope. (*B*) Chromatic aberration correction. Localization of the center of each spectrally separated PSF was determined by a Gaussian curve fitting using FISH_QUANT software (20); then all centroids were allocated in pairs, and distances were measured by using MATLAB custom algorithms (*Materials and Methods* and *SI Results*). A vector transformation map (affine transformation matrix) was used to then correct the images for chromatic aberration. Arrows illustrate displacement vectors. Yellow circles illustrate corrected images. (*C*) Objective contour distortion map of chromatic aberration. The actual distortion determined by the vector map in *B* for the specific objective used in this study. The entire FOV is represented (in nanometers). Vectors in black indicate chromatic shift direction and magnitude (Cy5 to Cy3). Cooler colors require minimal correction; warmer colors indicate major correction (in nanometers). (*D*) Percentages of colocalization between spectrally separated centroids before (black line) and after (red line) correction was applied to the entire FOV. (*E*) Distribution of observed distances of centroid pairs in two-color images after correction. Data are shown as gray bars, and the Gaussian fit is the red line. Mean of distribution = 7.86 ± 0.21 nm. Error, SEM.

with high affinity (14, 21, 22). To confirm the intracellular association between MCP-GFP and single–β-actin mRNA molecules within the cell, we performed single-molecule FISH in combination with immunofluorescence (smFISH-IF) in neurons (Fig. 2 *A* and *B*). We found that MBS (β-actin mRNA) molecules overlapped with MCP signal, both of which appeared as diffraction-limited spots. Neurons derived from WT mice were used as a negative control for MCP association because they have no MBS. We observed the MCP-GFP in the nucleus (MCP has a nuclear localization signal) of these lentivirus-infected WT neurons but

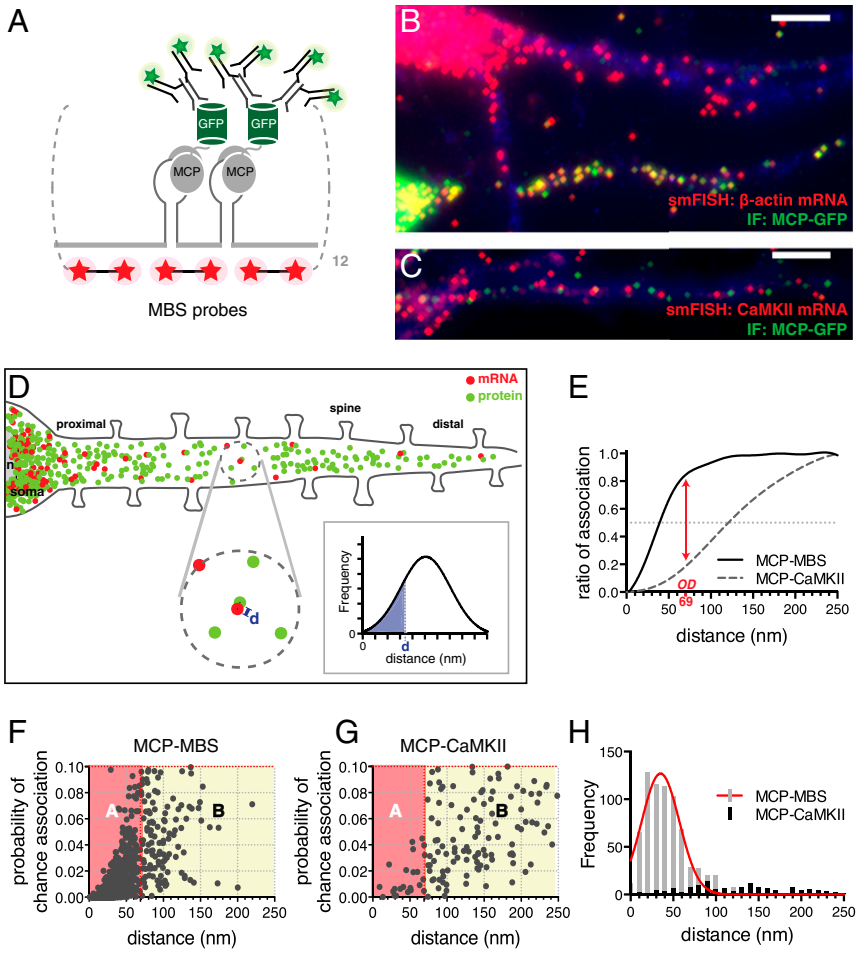

Fig. 2. Determining significance of association between MCP and endogenous MBS-containing β-actin mRNA. (*A*) Schematic representation of smFISH-IF on β-actin mRNP: 24 MBSs are present in β-actin 3′-UTR. Two MBSs separated by linker regions (gray) are illustrated for simplicity. Cy3-labeled RNA FISH probes (MBS probes are shown as red stars) hybridized to linker regions as described (18) are depicted. The MCP fused to GFP (gray circles and green barrels, respectively) is bound to the MBS as a dimer and can be detected by IF using antibodies against GFP and Alexa Fluor 647 (AF647)-conjugated secondary antibodies (illustrated with green stars). (*B* and *C*) Representative smFISH-IF images from dissociated hippocampal neurons from MBS mice expressing MCP-GFP by lentivirus infection were probed for (*B*) β-actin mRNA (MBS FISH probes, Cy3; red) or (*C*) CaMKII mRNA (CaMKII FISH probes, Cy3; red) and IF for MCP-GFP (GFP antibody, AF647; green). (*B*) A nonexpressing MCP-GFP neuron only showed FISH signal (red). MAP2 is shown in blue as a dendrite marker. (*C*) The image shows discrete fluorescent particles detected by both smFISH and IF throughout the dendrite that rarely overlap because the MCP does not bind CaMKII mRNA but binds β-actin mRNA with MBS in its 3′-UTR. Images are representative of four independent experiments, with over 15–20 dendrites observed in each experiment. (Scale bars: 5 μm.) (*D*) Schematic representation of a neuron and the super registration method that measures the significance of each mRNA–protein pair (red and green circles, respectively; magnified). The circle represents the nearest red circle (mRNA). The simulation measures the frequency that the number of green circles (protein) within this area would fall within distances less than *d* by chance. (*Inset*) The shaded area represents probability of chance association < 0.1 (the frequency for the illustrated pair based on 10,000 simulations). Every pair with this probability within 250 nm (the diffraction limit) is a single point in *F* and *G*. Complete data are in Fig. S2 *E* and *F*. (*E*) Curve of association between an mRNA and a binding protein was calculated as the cumulative ratio of association for intermolecular distances (in the range between 0 and 250 nm) that were less than a given observed distance. The ratio of association was calculated between the number of molecular pairs that can be found in proximity at each given nanometer of distance (and probability of chance association < 0.1) and the total number of molecular pairs within 250 nm (*F* and *G*). Red arrows show the distance wherein the mRNA–protein association for MCP-MBS and MCP-CaMKII is maximally separated [optimal distance (OD) = 69 nm] (*Materials and Methods*, *Measurement of Association*). Black line, MCP-MBS; dotted gray line, MCP-CaMKII. (*F* and *G*) Scatterplots show the probability of chance association between molecules for (*F*) MCP-GFP and β-actin mRNA (MBS) in MCP-MBS and (*G*) MCP-GFP and CaMKII mRNA (CaMKII) in MCP-CaMKII. Box A (pink) includes the associated molecules that have a probability of chance association < 0.1 and a distance less than the optimal distance of 69 nm (red vertical line; *E*). Box A includes the molecules that are physically likely to be in contact. Box B (light yellow) includes molecules with a probability of chance association < 0.1 but at distances greater than the optimal distance and within the diffraction limit of 250 nm. Box B includes the molecules that would be detected as positives by standard colocalization. The total numbers of intermolecular pairs in box A are 614 for MCP-MBS and 21 for MCP-CaMKII. The total numbers of pairs in box B are 120 for MCP-MBS and 111 for MCP-CaMKII (Fig. S2 *E* and *F*). (*H*) Distribution of observed distances for MCP-MBS (gray bars; Gaussian fit in red line) and MCP-CaMKII (MCP is bound to MBS on β-actin mRNA; black bars) after correction. Mean of observed distance was 34.58 ± 0.65 nm for MCP-MBS. Mean observed distance was 541.96 ± 8.14 nm for MCP-CaMKII (chance association) (Fig. S2*D*). Error, SEM.

did not observe any MCP-GFP spots in dendrites, confirming that its association with the mRNA was MBS-dependent (Fig. S2 *A–C*). These results indicate that both MCP-GFP (protein) and MBS (β-actin mRNA) are detected in close proximity within dendrites, consistent with their expected intermolecular interaction.

Redefining Colocalization: Significance of RNA–Protein Association. To ensure that the overlapping spots of single-molecule FISH (smFISH) to the MBS and immunofluorescence (IF) to the MCP-GFP did not occur by chance, we measured the likelihood of finding these two molecules in close proximity. To address this quantification, we included the negative control for RNA–protein association (in this case, MCP-GFP) and a dendritically localized transcript without MBS (CaMKII mRNA) (Fig. 2*C*). After performing smFISH-IF for CaMKII and MCP-GFP, we observed few events of close proximity between the two molecules at distances less than 150 nm compared with MBS and MCP-GFP (Fig. 2 *B* and *C* and Fig. S2*D*). At increasingly larger distances (>150 nm), the spots are more likely to overlap by chance. In addition, any colocalization above 150 nm is not only a random event but occurs at a distance that is not relevant for physical contact.

The higher the local molecular density, the more likely that any colocalization could occur by chance and hence, influence the level of specificity and significance for observed colocalization events. Therefore, we designed an analysis that accounted for the local density around each of the associated pairs of labeled molecules: in this case, mRNA (Fig. 2*D*, red in expanded circle) and protein (*Materials and Methods*, Fig. 2*D*, green in expanded circle, and *SI Results*). We compared the observed intermolecular distances for each pair with a simulated Monte Carlo random distribution of the two colors at similar concentrations. This procedure provided a measurement to evaluate the significance compared with a randomized distribution. We expressed this probability of chance association when the simulation yielded a distance that was less than the observed distance (Fig. 2*D*, *Inset*). The lower the probability of chance association, the higher the probability that the observed colocalization reveals an intermolecular association that is statistically significant. Consistent with this result, we found that most MCP-GFP and MBS signals showed a high significance (probability of chance association is <0.1). In contrast, most MCP-GFP and CaMKII signals did not show significant association (Fig. 2 *F* and *G* and Fig. S2 *E* and *F*).

To obtain this probability measurement, we calculated association between the two molecules as a function of their distances apart for positive and negative controls (*Materials and Methods*, Fig. 2*E*, and *SI Results*). For the positive control, 85% of the observed distances from the labeled probes to the MBS and from the antibodies to the MCP-GFP were within 69 nm. In contrast, 15% of the observed associations in the negative control (MCP-GFP and the CaMKII probes) occurred at this distance (Fig. 2*E*, black and dotted gray lines, respectively). The 69-nm cutoff was determined to be the optimal distance between molecules, where the difference between the detection of association for the positive control and the detection of association for the negative control was the greatest (Fig. 2*E*, red arrows). Within this distance, we defined a probability of chance association less than 10% (<0.1) that represented mRNA–protein molecules that were likely to interact (*Materials and Methods*, box A in Fig. 2 *F* and *G*, *SI Results*, and Fig. S2 *E–H*). In this analysis, we found that there were mRNA–protein molecules with a probability of chance association less than 10% (because they were increased relative to the negative control) but that they were not in relevant proximity for a molecular interaction (i.e., distances ranging from optimal distance to 250 nm; box B). For MCP-GFP and MBS, the mean observed distance was 34.58 ± 0.66 nm (Fig. 2*H*). This measurement includes the distance from the labeled antibodies detecting MCP-GFP to the labeled oligonucleotide probes used to detect β-actin mRNA (using MBS FISH probes). A molecular model for the physical association of MCP-GFP and MBS using available crystal structures in PyMOL indicated that the antibodies positioned the fluorescent label ~25 nm away from the MCP-GFP. This model supports the conclusion that standard wide-field microscopy is capable of resolving a bona fide mRNA–protein complex (Fig. 3).

The precision of the registration showed that physical distances between the location where the protein is positioned relative to the FISH probes could be mapped within 10–20 nm depending on their separation, showing that this approach can serve as a "molecular ruler" (*SI Results* and Fig. S3).

Application to the Interaction Between ZBP1 and Its mRNA Targets. We then tested this analytical technique on a bona fide endogenous complex: the well-characterized interaction between β-actin mRNA

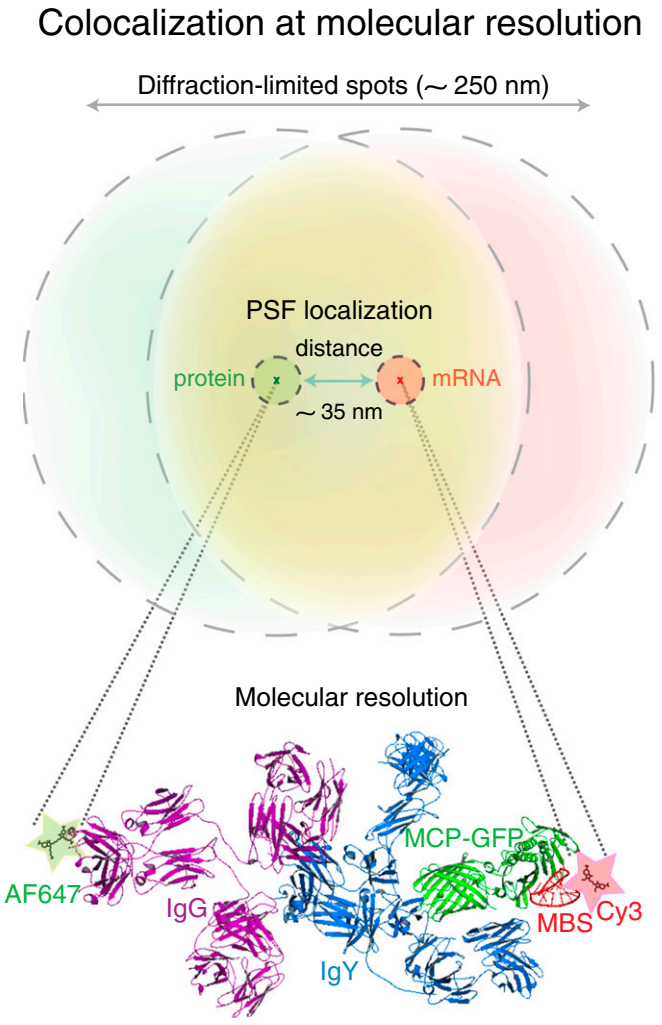

Fig. 3. Association between β-actin mRNA (MBS) and MCP as a molecular model mRNP. Schematic representation of overlapping red (RNA) and green (protein) diffraction-limited spots in a wide-field image and the molecular scale with nanometer precision of MCP-GFP and β-actin (MBS) interaction. By measuring and fitting a Gaussian curve to the PSF, the position in *x*, *y*, and *z* of its center can be determined accurately with high spatial resolution (compare outer dotted line with inner dotted line). One Cy3-labeled MBS (red), MCP-GFP (green), primary antibody (IgY; light blue), and Alexa Fluor 647-labeled secondary antibody (IgG; purple) are depicted. The mean observed distance between labeled antibody and labeled RNA FISH probes is 34.58 nm (Fig. 2*H*). The distance for MCP-GFP to β-actin mRNA is estimated at 7 nm. The drawing of the molecules was generated in PyMol software with the help of published structure data (22, 44).

and ZBP1, the protein that binds to its bipartite zipcode sequence element present in the 3′-UTR (14, 16). MBS neuronal cultures infected with lentivirus encoding GFP fused to ZBP1 showed discrete particles along mature dendrites, reminiscent of dendritically transported mRNA granules with different sizes and signal intensities (Fig. 4 *A* and *C* and Fig. S4 *A* and *F*). Analysis of the images revealed that the overlap between β-actin mRNA (FISH signal) and ZBP1-GFP (IF signal) was 27% (Fig. 4 *E* and *F* and Fig. S4 *B* and *D*). This association of ZBP1-GFP with the mRNA is less than that of MCP-GFP, which has essentially a longer off rate. Other than β-actin mRNA, other targets for ZBP1 have been described (16). For instance, spinophilin, a zipcode-containing mRNA, was enriched in pulldown experiments for ZBP1 from brain extracts and localized to mature dendrites dependent on ZBP1 (16). In support of this finding, we observed ZBP1-GFP in close proximity with spinophilin mRNA within mature dendrites (Fig. 4 *B*, *D*, *E*, and *G* and Fig. S4 *C*, *E*, and *F*). Our findings showed one population of interacting molecules from 0 to 69 nm and another from 69 to 100 nm, consistent with this mRNA having two putative zipcodes (Fig. 4 *B* and *G* and Fig. S4*F*). The ZBP1-GFP molecules bound to spinophilin mRNA molecules at optimal distance < 69 nm were greater than those bound to β-actin mRNA (using MBS FISH probes) (Fig. 4*E*). These results show that this imaging method has the resolution to determine where in the dendrite a direct interaction occurs between an RBP, such as ZBP1, and its mRNA targets and its relative degree of association compared with MBS-MCP.

Validation of β-Actin mRNA-Associated Factors. To evaluate the efficacy of this approach to validate putative RNA–protein interactions, we isolated additional binding proteins for β-actin mRNA by a typical pulldown assay. By using in vitro transcribed *Pseudomonas aeruginosa* PP7 bacteriophage (PP7)-tagged zipcode-containing β-actin 3′-UTR RNA as bait, we captured stably associated proteins from mammalian cell extracts (Fig. 5 *A* and *B*). Proteins specifically bound to β-actin 3′-UTR RNA were eluted, separated by SDS/PAGE, and analyzed by liquid chromatography–MS/MS (LC-MS/MS). Gene ontology analysis revealed that proteins found associated with β-actin 3′-UTR were principally involved in RNA posttranscriptional modification, protein synthesis, gene expression, and RNA trafficking functions (Dataset S1 and Fig. S5 *A* and *B*). In addition to ZBP1, we found heterogeneous nuclear ribonucleoproteins (hnRNPs) AB, A0, A3, A1, L, D, DL, UL1, U, Q1 (Syncrip), and R; Y-Box binding protein 1 (YBOX1); Cold shock domain-containing protein A; ATP-dependent RNA helicase A (Dhx9); IMP2; IIF2; Staufen 1 & 2; PABP1; Src-associated in mitosis 68 kDa (Sam68); Myelin expression factor 2-like; UPF1; eIF3; and several SR proteins. We also found the motor-related protein Myosin Regulatory Light Chain 2.

We confirmed the association between β-actin 3′-UTR RNA and proteins identified by standard biochemical techniques, such as Western blot (Fig. 5*C* and Fig. S5*C*) and RNA immunoprecipitation (RIP) (Fig. 5*D*). ZBP1, hnRNPAB (23), Dhx9, YBOX1, and Sam68 (24) showed a significant interaction with β-actin 3′-UTR RNA compared with the control RNA. Non-RBPs, such as tubulin or actin, were not detected in pulldown eluates, indicating enrichment in specific binders. FMRP, a prominent neuronal mRNA-binding protein (25), was not detected by either LC-MS/MS or Western blot analysis. While Western blots in Fig. 5*C* highlighted the specificity of protein–RNA interactions found by LC-MS/MS, endogenous β-actin mRNA was found in eluates of immunoprecipitations carried out by specific antibodies against Dhx9, hnRNPAB, and YBOX1 (Fig. 5*D*). Binding of ZBP1, hnRNPAB, YBOX1, and Sam68 was precluded when a β-actin 3′-UTR RNA containing a deletion of the zipcode sequence region was used, suggesting that they bound to the zipcode or were part of a zipcode binding complex (Fig. S6).

Finally, we tested the identified RNA–protein associations by super registration microscopy. YBOX1, Sam68, hnRNPE2, hnRNPU, hnRNPAB, and Dhx9 IF combined with smFISH for β-actin mRNA (using MBS FISH probes) was performed in fixed neurons, and intermolecular distances were calculated (Fig. 5 *E* and *F* and Figs. S5 *D*–*J* and S7 and Table S1). RNA–protein associations ranged from 10 to 40% for all of the identified factors analyzed with β-actin mRNA in hippocampal dendrites (Fig. 5*E* and Table S1). ZBP1, YBOX1, and Sam68 were associated with β-actin mRNA; however, Dhx9, hnRNPE2, hnRNPU, and hnRNPAB were nonspecific in their interactions, similar to the association of CaMKII (15%). We assumed similar molecular conformations and dye orientations for each pair and used the optimal distance less than 69 nm previously determined. Therefore, two-color imaging can critically evaluate whether single molecules of mRNA make bona fide physical contacts with putative binding proteins.

Discussion

In this study, we provide an approach to ascertain the physical interaction between single mRNAs and binding proteins in situ in single cells using standard wide-field microscopy. The flowchart is illustrated in Fig. 6. This imaging method extends biochemical-based studies on RNA–protein interactions by providing spatial information about where in the cells these interactions are likely to occur. This morphological information is especially important in neurons, in which RNA regulatory mechanisms play an essential role in the regulation of localized gene expression.

The analysis of colocalization has, as its basis, the likelihood of finding two molecules in close proximity. For instance, colocalization is deduced by the merging of two colors (e.g., a yellow spot when comparing red with green pseudocolors). However, a yellow spot may not indicate real association between molecules. First, the resolution may not be sufficient to determine the true distance between the colors. Second, the overlap may have occurred by chance dependent on the concentrations of each of the molecules. By this same reasoning, two molecules may be colocalized even if a merged signal is not apparent because of chromatic aberration or disparities in the brightness of each component. In this work, we have developed a quantitative image acquisition and analysis method that measures the distance between labeled molecules and the likelihood of their physical association independent of their intensities.

Various statistical methods have been proposed to address colocalization using single-molecule imaging. A dominant method is the Ripley's K function method (reviewed in ref. 26), which tests spatial randomness through the computation of its quantiles. This method and its derivatives have been developed to create a fast and robust statistical test. However, this approach is limited because the region of interest (ROI) requires straight lines at its edges to account for edge-effect biases and may not be as accurate as the more computationally expensive Monte Carlo simulation. Because neuronal structure is highly irregular and small sets of pairing events require quantitative characterization, we centered our study on the interaction between individual mRNAs and proteins without analyzing the global spatial molecule distribution through an ROI. Therefore, the imaging analysis described here allows an objective quantification of the probability of molecular association, and it is independent of the molecular density within the cell.

Chemical and UV cross-linking followed by RNA sequencing after immunoprecipitation has been used to identify putative mRNA–protein associations (27–32). However, although these techniques show that these molecules can interact, it does not provide evidence of a stable in vivo complex; the molecules may come in contact transiently on cell disruption or be artificially stabilized by cross-linking (33, 34). In contrast, imaging at the single-molecule and cellular level provides evidence of a biologically relevant interaction. In addition, the percentage binding can be represented spatially in unmodified cells: where in the cell this binding is likely to occur.

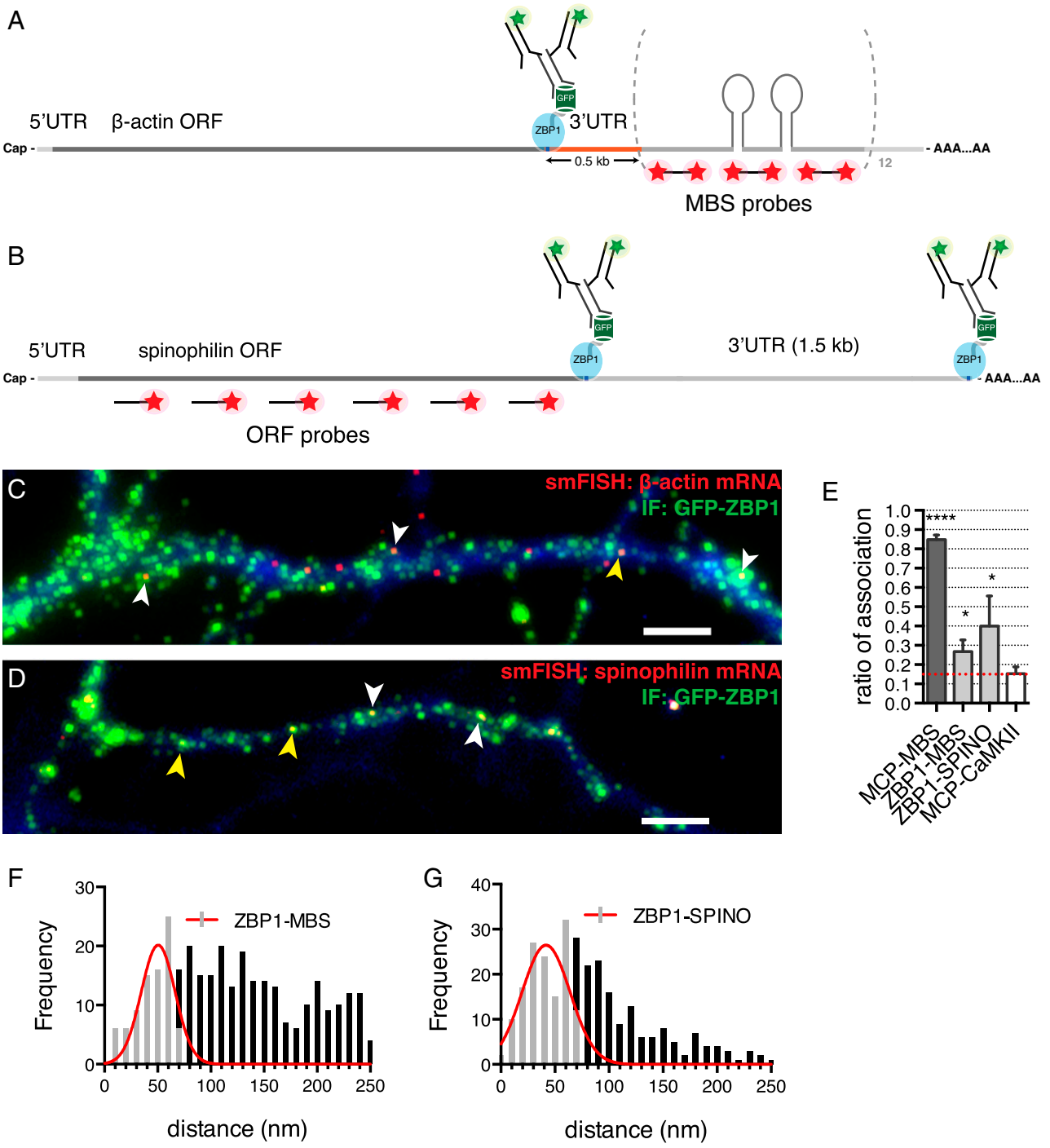

Fig. 4. Association between ZBP1 and endogenous mRNA targets at molecular resolution. (*A*) Schematic representation of β-actin mRNA showing MBS and the zipcode (blue) bound by ZBP1 (light-blue oval) in the 3′-UTR. Two MBSs separated by linker regions (gray) are illustrated for simplicity. Cy3-labeled RNA FISH probes (MBS probes; red stars) and antibodies are also depicted. (*B*) Schematic representation of spinophilin mRNA showing two putative zipcodes (blue) bound by ZBP1 (light-blue ovals) in the 3′-UTR. Cy3-labeled RNA FISH probes (red stars) and antibodies are also depicted. (*C* and *D*) Representative smFISH-IF images in dissociated hippocampal neurons from MBS mice expressing GFP-ZBP1 detected by GFP antibody (green) combined with smFISH for (*C*) β-actin mRNA (MBS FISH probes; red) and (*D*) spinophilin mRNA (red). Distal dendrites were analyzed where both smFISH and IF detected discrete fluorescent spots. Yellow arrowheads show sites of molecular interaction as defined by box A in Fig. 2 (probability of chance association < 0.1 and optimal distance = 69 nm); white arrowheads show nonassociated molecules as defined by box B in Fig. 2 (distances between optimal distance and 250 nm). MAP2 is shown in blue as a dendrite marker. Images are representative of (*C*) five and (*D*) two independent experiments, with over 20 dendrites observed in each experiment. (Scale bars: 5 μm.) (*E*) Ratios of association for ZBP1-MBS and ZBP1-SPINO in neurons compared with the standard model MCP-MBS and MCP-CaMKII (negative control). The dotted red line indicates background association as defined by MCP-CaMKII. Error bar, SD. Unpaired *t* test. $*P < 0.05$; $****P < 0.0001$. (*F* and *G*) Distribution of observed distances for GFP-ZBP1 and β-actin mRNA (ZBP1-MBS) in *F* and GFP-ZBP1 with spinophilin mRNA (ZBP1-SPINO) in *G* after correction. Gray bars and red lines show associated molecules as defined by box A (optimal distance < 69 nm); black bars show nonassociated molecules as defined by box B (distances between optimal distance and 250 nm). Mean of observed distance was 45.44 ± 1.80 nm for ZBP1-MBS in *F* and 41.00 ± 1.53 nm for ZBP1-SPINO in *G*. Error, SEM.

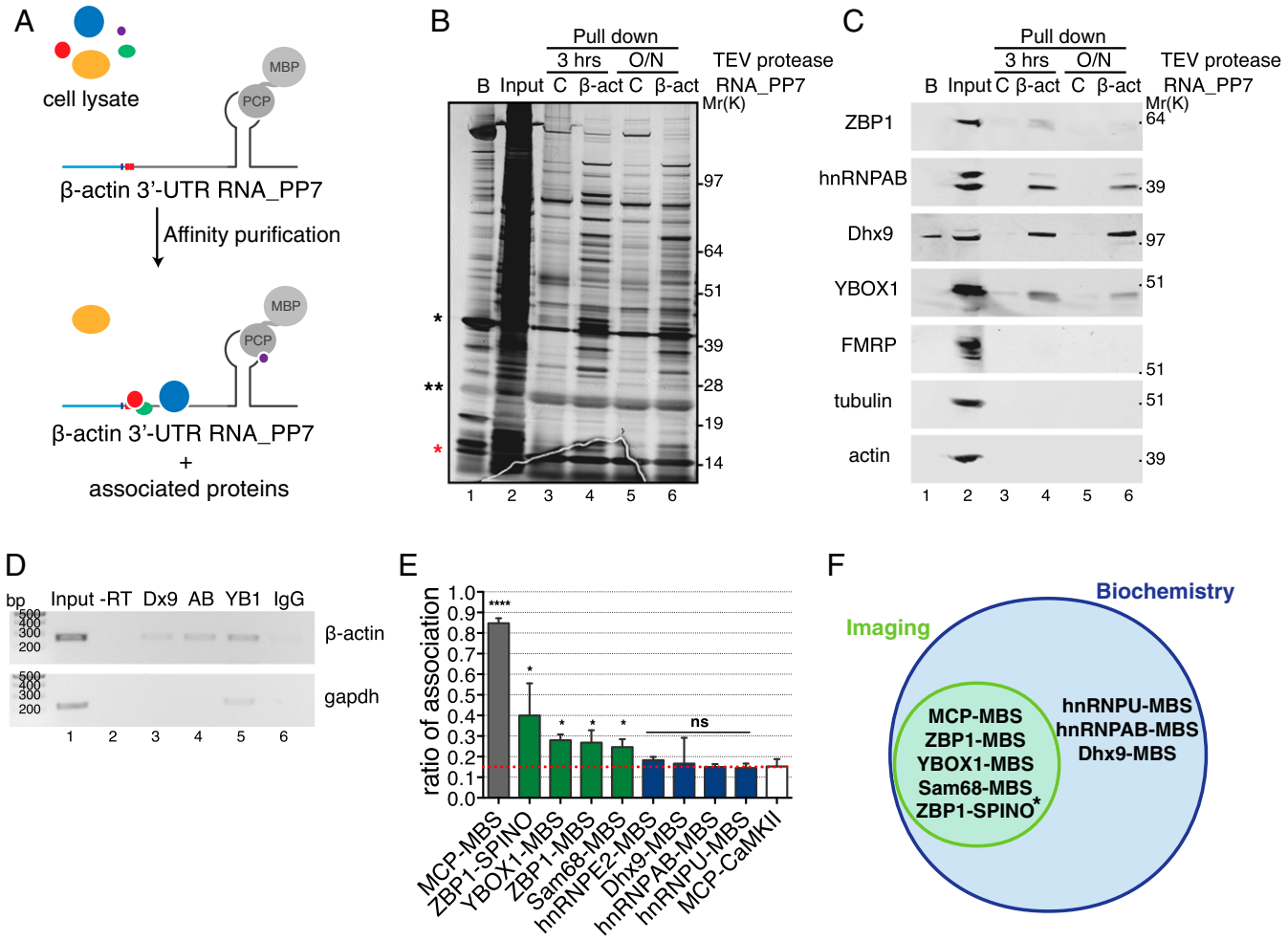

Fig. 5. Validation of β-actin 3′-UTR affinity purification of associated proteins. (*A*) Schematic representation of β-actin 3′-UTR pulldown strategy. In vitro-transcribed PP7-tagged zipcode-containing β-actin 3′-UTR RNA was incubated with mouse embryonic fibroblast cell lysates, affinity-purified on amylose magnetic resin, and incubated with TEV protease either for 3 h or overnight (O/N) to identify protein components that interact with β-actin mRNA and ZBP1 protein. β-Actin 3′-UTR containing one PP7 binding site (gray) bound by PP7 coat protein (PCP) fused to MBP (gray circles), the zipcode element (red), and the coding region (light blue) are depicted. (*B*) Silver-stained SDS/PAGE gel of proteins specifically bound to β-actin 3′-UTR RNA isolated from mouse embryonic fibroblast extracts using either a control (C; lanes 3 and 5) or β-actin 3′-UTR (lanes 4 and 6) as a bait. A list of proteins identified by LC-MS/MS is summarized in Fig. S5*B* and Dataset S1. Molecular weight (M_r) is shown. Beads (B; lane 1) indicate proteins remained bound to beads after TEV elution. Input (lane 2) indicates 3 μg total protein. Lanes 3–6 show 60% of pulldown eluates. Red asterisk indicates PCP. *MBP-PCP; **TEV protease. (*C*) Western blot analyses of indicated proteins in input and pulldown eluates on TEV protease digestion for 3 h or overnight (O/N) as indicated. Molecular weight (M_r) is shown. Beads (B; lane 1) indicate proteins that remained bound to beads after TEV elution. Input (lane 2) indicates 30 μg total protein. Lanes 3–6 show 40% of pulldown eluates. The results shown are representative of three independent experiments. (*D*) RIP. Enrichment of (*Upper*) endogenous β-actin and (*Lower*) GAPDH mRNAs in Dhx9 (Dx9), hnRNPAB (AB), and YBOX1 (YB1) immunoprecipitations (lanes 3–5) compared with IgG control (lane 6). A PCR carried out without reverse transcriptase (–RT) is shown in lane 2. (*E*) Summary of association of the indicated mRNA and proteins by smFISH-IF in dendrites. Dotted red line indicates background association defined by MCP-CaMKII. Error bar, SD. Unpaired *t* test; ns indicates $P > 0.05$. *$P < 0.05$; ****$P < 0.0001$. (*F*) Venn diagram showing mRNA and protein association validated by both imaging and biochemistry approaches in this work. *mRNA–protein association validated by biochemistry in ref. 16.

This imaging method can characterize and validate protein components of a specific messenger ribonucleoprotein (mRNP). In addition to the well-known ZBP1, we found other proteins that bound to the zipcode-containing β-actin 3′-UTR using a PP7 stem loop to pull down the RNA. From the list of protein candidates that bound the β-actin 3′-UTR, the presence of YBOX1, hnRNPAB, and Dhx9 was consistent with its presence in ZBP1/IMP1 ribonucleoprotein particle (RNP) granules (35, 36). Sam68 has also previously been found to bind to β-actin mRNA in neurons and regulate its translation (24, 37, 38). More importantly, the approach will be instrumental in ruling out false positive associations. For instance, hnRNPAB has been shown to bind AU-rich response elements commonly present in 3′-UTRs (39–42), and we find it associated with β-actin 3′-UTR by affinity purification. However, this approach reveals that hnRNPAB and β-actin mRNA do not interact except by chance in dendrites. Similarly, hnRNPU and Dhx9, an RNA helicase mostly enriched in the nucleus, also do not associate with β-actin mRNA except by accident in dendrites in contrast to results that suggested specific binding using biochemical techniques (Fig. 5 and Table S1). It should be noted, however, that the observations do not negate the possibility of a physiologically significant effect of these proteins because a transient interaction may be sufficient for a protein to modify an RNA or promote formation of a complex, even if the interaction occurs statistically by chance. Nonetheless, this method clearly identifies proteins (ZBP1, YBOX1, and Sam68) that are stably associated with β-actin mRNA at intermolecular distances below 69 nm, the threshold for distinguishing physically meaningful interactions. However, it is also possible that proteins in a large complex (>69 nm) may be associated but may not be in

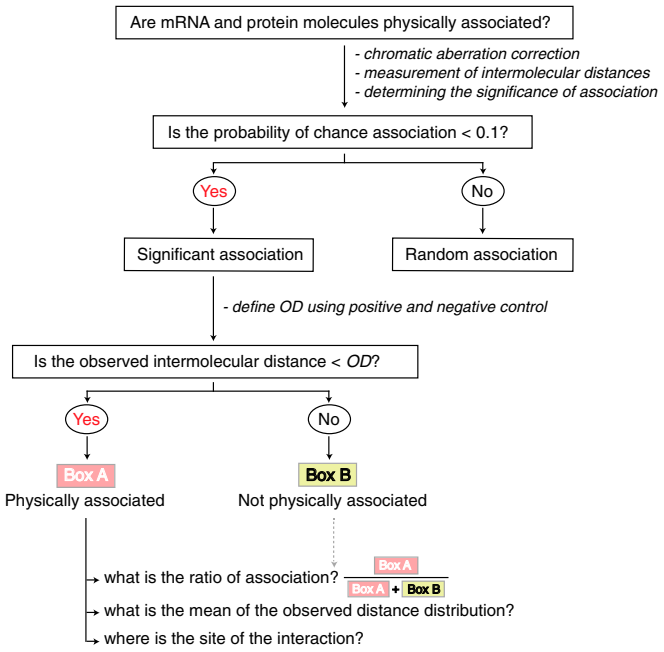

Fig. 6. Flowchart illustrating the steps to determine whether mRNA and protein molecules physically interact within cells. OD, optimal distance.

physical contact with the mRNA. In addition, the association of ZBP1-GFP with β-actin mRNA may be underestimated because there was competition with the endogenous ZBP1 for β-actin mRNA binding. ZBP1 also dissociates from the mRNA depending on its phosphorylation (15, 43). Finally, the detection of the ZBP1-GFP by antibodies would be less efficient than direct labeling of mCherry-ZBP1 in cells derived from a KO mouse, where all ZBP1 is labeled (43).

Identifying bona fide RNA–protein associations in situ is important for investigating their roles in a variety of molecular and subcellular events, such as local translation in synaptic plasticity. The RNA–protein interactome can be explored with the methodology described here. smFISH-IF can be generally applied to any combination of mRNA and binding protein(s), allowing single mRNP complex observation at cellular sites of mRNP assembly. Notably, endogenous mRNAs and proteins can be directly investigated by using RNA FISH probes and antibodies commercially available without genetic manipulation of the cells. Importantly, this approach can be achieved by simple fluorescence microscopes and does not require laser illumination, EM-CCD cameras, long imaging acquisition times, deconvolution, or image reconstruction. Thus, this imaging method will be an essential technique to complement biochemical studies because the spatial relationship within the cell is preserved.

Materials and Methods

Mouse Hippocampal Neuron Culture. Animal work was performed in accordance with Institutional Animal Care and Use Committee protocols at the Albert Einstein College of Medicine. Postnatal mouse hippocampal tissue was isolated from homozygous MBS knock-in (18) newborn pups (P0–P1). Hippocampi were placed in 0.25% trypsin for 15 min at 37 °C. Tissue was triturated, plated onto poly–D-lysine (Sigma-Aldrich)–coated glass-bottom dishes (MatTek) at 45,000 cells per dish, and cultured in Neurobasal A Media (Life Technologies) supplemented with B-27 (Life Technologies), GlutaMax (Life Technologies), and Primocin (InvivoGen). Hippocampal neurons from WT mouse embryos [embryonic day (E) 18; BrainBits, LLC] were prepared as above. Dissociated mouse hippocampal neurons were infected with lentivirus expressing MCP-GFP or ZBP1-GFP at 5 d in vitro.

smFISH-IF. Combining smFISH with IF required multiple conditions to accommodate both reagents. For fixation, permeabilization, and staining, mouse postnatal hippocampal neuronal cells infected on DIV5 with lentivirus encoding for tandem dimer MCP-GFP were fixed at DIV14–DIV21 with ice-cold 4% (vol/vol) paraformaldehyde and 4% (wt/vol) sucrose in 1× PBS supplemented with 1 mM $MgCl_2$ and 0.1 mM $CaCl_2$ (PBS-MC) for 20 min, quenched in 50 mM glycine, and permeabilized with ice-cold 0.1% Triton X-100 (28314; Thermo Scientific) and 0.5% UltraPure BSA (AM2616; Life Technologies) in 1× PBS-MC for 15 min. After incubation with 10% (vol/vol) formamide, 2× SSC, and 0.5% UltraPure BSA in RNase-free water for 30 min at room temperature, cells were incubated for 3 h at 37 °C with either 10 ng (Invitrogen) or 50 nM (Stellaris RNA FISH Probes; Biosearch Technologies) labeled mix probe sets (Dataset S2) and primary antibody against GFP from Aves Labs, Inc. (GFP-1010) at 1/5,000 dilution in Hybridization Buffer [10% formamide, 1 mg/mL *Escherichia coli* tRNA, 10% dextrane sulfate, 20 mg/mL BSA, 2× SSC, 2 mM Vanadyl Ribonucleoside Complex, 10 U/mL Superase.In (Ambion) in RNase-free water]. Then, cells were quickly washed and incubated twice with Alexa Fluor 647-conjugated secondary antibody (Life Technologies) at 1/1,000 dilution in 10% formamide and 2× SSC in RNase-free water for 20 min at 37 °C. After four 2× SSC washes, DNA was counterstained with DAPI (0.5 μg/mL in 2× SSC; Sigma-Aldrich), and after a final wash, cells were mounted using ProLong Gold Antifade Reagent (Life Technologies). smFISH-IF spot signals were dilated by one pixel for visualization.

Microscope Setup. Images were taken using an upright, wide-field Olympus BX-63 Microscope equipped with a SuperApochromatic 60×/1.35 N.A. Olympus Objective (UPLSAPO60XO), an X-Cite 120 PC Lamp (EXFO), an ORCA-R2 Digital Interline CCD Camera (C10600-10B; Hamamatsu) mounted using U-CMT and 1X-TVAD Olympus c-Mount Adapters, and zero-pixel shift filter sets: DAPI-5060C-Zero, FITC-5050A-Zero, Cy3-4040C-Zero, and Cy5-4040C-Zero from Semrock. The resulting image pixel size was 107.5 nm, and the *z*-step size (along the optical axis) used for all optical sectioning acquisition was 200 nm. To position the specimen more accurately along the optical axis (in *z*) and minimize mechanical vibration, a PZMU-2000 Piezo-Z Top Plate from Applied Scientific Instrumentation was used. A webcam was used to monitor the automated acquisition remotely to avoid turbulence and temperature fluctuations in the microscope environment. To improve optical stability, we used a vibration isolation table (TMC) and ensured that airflow did not affect the microscope stand. The environmental control system maintained constant temperature (20 °C ± 1 °C) and low humidity (35 ± 5% relative humidity) during a given experimental day. Metamorph software (Molecular Devices) was used for controlling microscope automation and image acquisition.

Super Registration. We compensated for the objective's chromatic aberration across the entire FOV using a map that described the optical distortion as a function of position by observing subdiffraction limit-sized fluorescent beads that have broad emission spectra (TetraSpeck Fluorescent Microspheres, 100-nm diameter; Life Technologies). Multiple fields of beads ($n = 760$ beads) were imaged in three dimensions sequentially in Cy5 and Cy3 channels. Then, centroids of the PSF of the beads were localized with subpixel precision in each channel (*Materials and Methods*, *Single-Molecule Localization*). The Cy5 channel centroid positions in *x* and *y* were compared with the Cy3 channel centroid positions in *x* and *y*, and the displacement vectors between the centroid positions of each bead in the two channels were calculated. The displacement vectors were determined in each orthogonal axis independently as a function of the position in the FOV. The objective's chromatic aberration between Cy5 and Cy3 was compensated for using an affine transformation. A detailed description of the super registration can be found in *SI Results*.

Bead Preparation. Beads were diluted with distilled water and uniformly suspended by sonication before they were loaded to a poly–L-lysine–coated coverslip. After the beads settled and dried, Prolong Gold Mounting Media Reagent (Life Technologies) was added and left overnight on a level surface in the dark, and then the coverslip was sealed with nail polish.

Objective Testing. The optical calibration on six matched objectives acquired from Olympus was tested. All of these 60× objective lenses showed unique variations in their chromatic aberrations. Each objective lens was unique, in that its performance characteristics had its own "fingerprint" for optical distortion across the FOV. The objective that required the least total chromatic correction in our optical path was used for this study (UPLSAPO60XO, 4K020 serial number).

Single-Molecule Localization. To determine the centroid position of single molecules, we used FISH_QUANT software (20) (free and available online). Briefly, after background subtraction, the software fitted a 3D Gaussian function to the PSF of the single molecule, which yielded centroid coordinates in each channel with subpixel accuracy (<20 nm). Autofluorescent and

nonspecific signal were excluded by thresholding the intensity and by the width of the 3D Gaussian curve.

Measurement of Intermolecular Distances and Determining the Significance of Association. Software was written in MATLAB (MathWorks) to identify centroid pairs using nearest neighbor algorithm (pairing), measure intermolecular distances (in nanometers), and provide significance of association for each pair of molecules between the two channels. The method determined the probability of chance association for each intermolecular pair based on the intermolecular distances observed and the local molecular density within the cell. Details are in *SI Results*.

Measurement of Association. The following procedure determined the largest distance that two molecules could be separated and still be considered physically associated. First, the intermolecular distances and significance of association from a positive and negative control were calculated [in this case, MCP-GFP and MBS (MCP-MBS) and MCP-GFP and CaMKII (MCP-CaMKII), respectively (as described above in *Materials and Methods*, *Measurement of Intermolecular Distances and Determining the Significance of Association*)]. Second, the molecular pairs that exhibited the most significant probability of chance association (<0.1) and that had a intermolecular distance < 250 nm (diffraction limit) were selected. The cumulative ratio of association for intermolecular distances (in the range between 0 and 250 nm) that were less than or equal to a given observed distance was plotted (for both positive and negative controls separately) (Fig. 2*E*). The distance wherein the difference was the highest between the detection of association for MCP-MBS ("signal") and the detection of association for MCP-CaMKII ("noise") defined the optimal distance (in this case, 69 nm) (Fig. 2*E*, red arrows). At the optimal distance, the signal to noise ratio is maximized. Thus, we used the distance of 69 nm as the optimal distance in the analysis of RNA–protein interaction unless otherwise noted. Only the molecular pairs with probability of chance association < 0.1 and intermolecular distances less than optimal distance were considered associated and defined the population of pairs included in box A (Fig. 2 *F* and *G*). Box B was defined as the population of molecular pairs with probability of chance association < 0.1 but at intermolecular distances in the range from the optimal distance to 250 nm. Finally, the ratio of association between molecules of mRNA and protein was expressed as the ratio of the population of box A to the population of boxes A and B combined. Optimal distance is dependent on both the positive and negative controls analyzed.

The interacting labeled molecules included in box A showed intensities that were representative of the total molecular population analyzed (Fig. S2 *G* and *H*). This result indicates that this imaging is able to identify bona fide mRNA–protein associations based on the spatial position of their fluorophores, independent of their intensities.

Imaging Analysis Software. All image analysis was performed with existing software packages and custom algorithm programs written in MATLAB (MathWorks). The code provides (*i*) chromatic aberration and mechanical shift corrections (super registration), (*ii*) identification of centroid pairs (pairing) and measurement of intermolecular distances (in nanometers), (*iii*) evaluation of the probability of chance association, and (*iv*) ratio of association as described in this work. The software is able to read FISH_QUANT (20)-detected spot files (version 3D_v1) and import all of the centroid positions in *x* and *y* along with the corresponding ROI chosen. It can import as many ROIs as the image has at once. The code (version 1.0) is available online through our website (open access for anyone to use without restriction).

PP7-Based RNA Affinity Purification (Pulldown). Amylose magnetic resin (NEB) was washed twice and incubated with recombinant purified protein Maltose Binding Protein (MBP)-PP7 and preheated PP7–β-actin 3′-UTR RNA (ratio 1:1) in binding buffer [20 mM Tris, pH 7.2, 200 mM NaCl, 1 mM EDTA, pH 8.0, 1 mM DTT, 0.01 mg/mL tRNA, 0.01% IGEPAL CA-630 (Sigma-Aldrich)] for 1 h at 4 °C with constant rotation. The pulldown was then performed by adding cell extract aliquots (5–30 mg total protein) supplemented with 100 mM NaCl and 0.01 mg/mL tRNA to the RNA immobilized to the beads through the MBP-PP7 protein followed by incubation at 4 °C for 2 h with constant rotation. Total protein aliquots used in pulldown procedures varied and are listed in figures. We use 1.5-mL nonstick microcentrifuge tubes when working with small volumes or 15-mL sterile polypropylene centrifuge tubes with larger volumes. After pulldown, the magnetic beads were washed five times (1-mL volume washes) with ice-cold wash buffer (20 mM Tris, pH 7.2, 200 mM NaCl, 1 mM EDTA, pH 8.0, 1 mM DTT, 0.01% IGEPAL CA-630) and transferred to a new tube in the last wash step. For RNP complex elution from the beads, Tobacco Etch virus (TEV) protease was added to the beads followed by 3 h of incubation at 4 °C with rotation. Alternatively, 500 μL 0.5 M NH_4OH supplemented with 0.5 mM EDTA, pH 8.0, was added to the beads followed by a 20-min incubation at room temperature with rotation. After beads were removed, eluate fractions were lyophilized in the Eppendorf Vacufuge speed vac for at least 4 h at room temperature. For protein analysis using SDS/PAGE, the eluates were incubated with appropriate volume of 4× protein sample buffer (Invitrogen) supplemented with 50 mM DTT and heated at 70 °C for 10 min. Construction of the PP7-tagged β-actin 3′-UTR RNA, PP7-MBP recombinant protein purification, and cell extract preparation can be found in *SI Materials and Methods*.

Additional information includes *SI Materials and Methods*, *SI Results*, Datasets S1 and S2, Figs. S1–S7, and Table S1.

ACKNOWLEDGMENTS. We thank Jeff A. Chao for the MBP-PP7 recombinant protein and 3′-UTR β-actin_PP7 construct; Xiuhua Meng for GFP-ZBP1 cloning; Jeetayu Biswas for the molecular model in PyMOL; Young Yoon for hippocampal neuron cultures and discussion; Bin Wu for tdMCP-GFP lentivirus and discussion; Chiso Nwokafor and Melissa Lopez-Jones for mice; Aviv Bergman for mathematical modeling; Stefan Hüttelmaier for anti-zbp1, anti-hnRNPU, and anti-hnRNPE2 antibodies; Maria Vera and members of the R.H.S. laboratory for critical reading of the manuscript; Joe Fernandez and Milica Tesic Mark for proteomics (Rockefeller University); and Andrew Gerson (Olympus) and Thomas Geer (BioVision) for help with instrumentation. This work was supported by a Human Frontier Science Program Fellowship (to C.E.), NIH Grant NS083085 (to R.H.S.), and the Integrated Imaging Program of the Gruss Lipper Biophotonics Center.

1. Eliscovich C, Buxbaum AR, Katz ZB, Singer RH (2013) mRNA on the move: The road to its biological destiny. *J Biol Chem* 288(28):20361–20368.
2. Glisovic T, Bachorik JL, Yong J, Dreyfuss G (2008) RNA-binding proteins and post-transcriptional gene regulation. *FEBS Lett* 582(14):1977–1986.
3. Kao DI, Aldridge GM, Weiler IJ, Greenough WT (2010) Altered mRNA transport, docking, and protein translation in neurons lacking fragile X mental retardation protein. *Proc Natl Acad Sci USA* 107(35):15601–15606.
4. King OD, Gitler AD, Shorter J (2012) The tip of the iceberg: RNA-binding proteins with prion-like domains in neurodegenerative disease. *Brain Res* 1462:61–80.
5. Lagier-Tourenne C, Polymenidou M, Cleveland DW (2010) TDP-43 and FUS/TLS: Emerging roles in RNA processing and neurodegeneration. *Hum Mol Genet* 19(R1): R46–R64.
6. Liu-Yesucevitz L, et al. (2011) Local RNA translation at the synapse and in disease. *J Neurosci* 31(45):16086–16093.
7. Lukong KE, Chang KW, Khandjian EW, Richard S (2008) RNA-binding proteins in human genetic disease. *Trends Genet* 24(8):416–425.
8. Nussbacher JK, Batra R, Lagier-Tourenne C, Yeo GW (2015) RNA-binding proteins in neurodegeneration: Seq and you shall receive. *Trends Neurosci* 38(4):226–236.
9. Paronetto MP, Achsel T, Massiello A, Chalfant CE, Sette C (2007) The RNA-binding protein Sam68 modulates the alternative splicing of Bcl-x. *J Cell Biol* 176(7):929–939.
10. Cook KB, Hughes TR, Morris QD (2015) High-throughput characterization of protein-RNA interactions. *Brief Funct Genomics* 14(1):74–89.
11. Oeffinger M (2012) Two steps forward–one step back: Advances in affinity purification mass spectrometry of macromolecular complexes. *Proteomics* 12(10):1591–1608.
12. Mili S, Steitz JA (2004) Evidence for reassociation of RNA-binding proteins after cell lysis: Implications for the interpretation of immunoprecipitation analyses. *RNA* 10(11): 1692–1694.
13. Riley KJ, Steitz JA (2013) The "Observer Effect" in genome-wide surveys of protein-RNA interactions. *Mol Cell* 49(4):601–604.
14. Chao JA, et al. (2010) ZBP1 recognition of beta-actin zipcode induces RNA looping. *Genes Dev* 24(2):148–158.
15. Hüttelmaier S, et al. (2005) Spatial regulation of beta-actin translation by Src-dependent phosphorylation of ZBP1. *Nature* 438(7067):512–515.
16. Patel VL, et al. (2012) Spatial arrangement of an RNA zipcode identifies mRNAs under post-transcriptional control. *Genes Dev* 26(1):43–53.
17. Ross AF, Oleynikov Y, Kislauskis EH, Taneja KL, Singer RH (1997) Characterization of a beta-actin mRNA zipcode-binding protein. *Mol Cell Biol* 17(4):2158–2165.
18. Lionnet T, et al. (2011) A transgenic mouse for in vivo detection of endogenous labeled mRNA. *Nat Methods* 8(2):165–170.
19. Bertrand E, et al. (1998) Localization of ASH1 mRNA particles in living yeast. *Mol Cell* 2(4):437–445.
20. Mueller F, et al. (2013) FISH-quant: Automatic counting of transcripts in 3D FISH images. *Nat Methods* 10(4):277–278.
21. Wu B, Chao JA, Singer RH (2012) Fluorescence fluctuation spectroscopy enables quantitative imaging of single mRNAs in living cells. *Biophys J* 102(12):2936–2944.
22. Chao JA, Patskovsky Y, Almo SC, Singer RH (2008) Structural basis for the coevolution of a viral RNA-protein complex. *Nat Struct Mol Biol* 15(1):103–105.
23. Sinnamon JR, Waddell CB, Nik S, Chen EI, Czaplinski K (2012) Hnrpab regulates neural development and neuron cell survival after glutamate stimulation. *RNA* 18(4): 704–719.
24. Klein ME, Younts TJ, Castillo PE, Jordan BA (2013) RNA-binding protein Sam68 controls synapse number and local β-actin mRNA metabolism in dendrites. *Proc Natl Acad Sci USA* 110(8):3125–3130.

25. Bassell GJ, Warren ST (2008) Fragile X syndrome: Loss of local mRNA regulation alters synaptic development and function. *Neuron* 60(2):201–214.
26. Lagache T, Sauvonnet N, Danglot L, Olivo-Marin JC (2015) Statistical analysis of molecule colocalization in bioimaging. *Cytometry A* 87(6):568–579.
27. Ule J, et al. (2003) CLIP identifies Nova-regulated RNA networks in the brain. *Science* 302(5648):1212–1215.
28. Hafner M, et al. (2010) Transcriptome-wide identification of RNA-binding protein and microRNA target sites by PAR-CLIP. *Cell* 141(1):129–141.
29. Ule J, Jensen K, Mele A, Darnell RB (2005) CLIP: A method for identifying protein-RNA interaction sites in living cells. *Methods* 37(4):376–386.
30. Licatalosi DD, et al. (2008) HITS-CLIP yields genome-wide insights into brain alternative RNA processing. *Nature* 456(7221):464–469.
31. Zhang C, Darnell RB (2011) Mapping in vivo protein-RNA interactions at single-nucleotide resolution from HITS-CLIP data. *Nat Biotechnol* 29(7):607–614.
32. König J, et al. (2010) iCLIP reveals the function of hnRNP particles in splicing at individual nucleotide resolution. *Nat Struct Mol Biol* 17(7):909–915.
33. Friedersdorf MB, Keene JD (2014) Advancing the functional utility of PAR-CLIP by quantifying background binding to mRNAs and lncRNAs. *Genome Biol* 15(1):R2.
34. Castello A, et al. (2012) Insights into RNA biology from an atlas of mammalian mRNA-binding proteins. *Cell* 149(6):1393–1406.
35. Jønson L, et al. (2007) Molecular composition of IMP1 ribonucleoprotein granules. *Mol Cell Proteomics* 6(5):798–811.
36. Weidensdorfer D, et al. (2009) Control of c-myc mRNA stability by IGF2BP1-associated cytoplasmic RNPs. *RNA* 15(1):104–115.
37. Lin Q, Taylor SJ, Shalloway D (1997) Specificity and determinants of Sam68 RNA binding. Implications for the biological function of K homology domains. *J Biol Chem* 272(43):27274–27280.
38. Itoh M, Haga I, Li QH, Fujisawa J (2002) Identification of cellular mRNA targets for RNA-binding protein Sam68. *Nucleic Acids Res* 30(24):5452–5464.
39. Snee M, Kidd GJ, Munro TP, Smith R (2002) RNA trafficking and stabilization elements associate with multiple brain proteins. *J Cell Sci* 115(Pt 23):4661–4669.
40. Raju CS, et al. (2011) In neurons, activity-dependent association of dendritically transported mRNA transcripts with the transacting factor CBF-A is mediated by A2RE/RTS elements. *Mol Biol Cell* 22(11):1864–1877.
41. Raju CS, et al. (2008) In cultured oligodendrocytes the A/B-type hnRNP CBF-A accompanies MBP mRNA bound to mRNA trafficking sequences. *Mol Biol Cell* 19(7):3008–3019.
42. Fukuda N, et al. (2013) The transacting factor CBF-A/Hnrnpab binds to the A2RE/RTS element of protamine 2 mRNA and contributes to its translational regulation during mouse spermatogenesis. *PLoS Genet* 9(10):e1003858.
43. Wu B, Buxbaum AR, Katz ZB, Yoon YJ, Singer RH (2015) Quantifying protein-mRNA interactions in single live cells. *Cell* 162(1):211–220.
44. Xu D, Jaroszewski L, Li Z, Godzik A (2014) AIDA: Ab initio domain assembly server. *Nucleic Acids Res* 42(Web Server issue):W308–W313.